Draft version April 15, 2016
Preprint typeset using LaTeX style AASTeX6 v. 1.0

arXiv:1604.03975v1 [astro-ph.GA] 13 Apr 2016

THE IONIZATION STRUCTURE OF SHARPLESS 2-264: MULTIWAVELENGTH OBSERVATIONS OF THE λ Ori H II REGION

M. Sahan
Department of Physics, University of Osmaniye Korkut Ata, Osmaniye, 80000, Turkey

L. M. Haffner
Department of Astronomy, University of Wisconsin, 475 North Charter Street, Madison, WI 53706
and
Space Science Institute, 4750 Walnut Street, Suite 205, Boulder, CO 80301

ABSTRACT

We present velocity-resolved maps taken with the Wisconsin H-Alpha Mapper (WHAM) in Hα, [S II] λ6716, and [N II] λ6583 around the well-known O8 III star λ Ori A (HD 36861) ($\ell = 185^\circ$ to 205°, $b = -24^\circ$ to -1°). The integrated intensity ($v_{\rm LSR} = -80$ to $+80$ km s^{-1}), $I_{\rm H\alpha}$, within WHAM's one-degree beams varies from ~ 190 R near the center to ~ 10 R on the periphery of the nebula where it becomes comparable to foreground and/or background emission in this complex region. Intensity ratios for [N II]/Hα and [S II]/Hα average 0.28 and 0.35, respectively. In both ratios, higher values are found preferentially at larger radii from λ Ori, although the behavior of [N II]/Hα is complicated near the edges of the nebula. The [S II]/[N II] intensity ratio ranges from ~ 0.5 to ~ 1.0, with the value increasing toward larger radii (and lower Hα intensities). Variations of [S II]/Hα, [N II]/Hα, and [S II]/[N II] line ratios in this diffuse region show some similar trends to those seen in the warm ionized medium (WIM) but with generally lower metal-line ratios. As with the WIM, the trends are driven by changes in the underlying physical parameters, most notably the ionization states and gas temperature. To investigate which cause might be dominant in this region, we use these extremely high signal-to-noise observations to construct a map of temperature and non-thermal velocity throughout the nebula. Using the line widths of Hα and [S II], we separate thermal and non-thermal components and find spatial trends of these parameters within the nebula. Ion temperatures range between 4000 K and 8000 K throughout the nebula. The non-thermal velocity map reveals a decrease in velocity from about 10 km s^{-1} to 5 km s^{-1} from the center to the edge of the lower half of the H II region. In addition to using the widths as a measure of temperature, we also use the variation in [N II]/Hα to estimate electron temperature. The results obtained from this diffuse H II region around λ Ori can be compared to studies of the WIM to provide important insight into the nature of the diffuse ionized gas (DIG) throughout the disk and halo of the Galaxy.

Keywords: H II regions — ISM: structure — ISM: individual (Sh 2-264) — ISM: atoms — stars: individual (HD 36861)

1. INTRODUCTION

The Wisconsin H-Alpha Mapper (WHAM) has measured a variety of optical emission lines for a multitude of large-scale ionized structures that include loops, filaments, and bubbles. The results from such studies provide insight into the workings of these discrete structures as well as the warm ionized medium (WIM) that pervades the Galaxy. The unique design of its 15-cm dual-etalon Fabry-Perot spectrometer allows WHAM to produce the first kinematic Hα map of the ionized gas in the Milky Way (Haffner et al. 2003) as well as spectral maps of diagnostic lines such as [S II] λ6716, [N II] λ6583, and [O III] λ5007 (e.g., Haffner et al. 1999; Madsen et al. 2006). Other recent large-angle surveys that

msahan2000@yahoo.com
haffner@astro.wisc.edu

trace diffuse Hα in our region of study include the Southern Hα Sky Survey Atlas (SHASSA; Gaustad et al. 2001) and the Virginia Tech Spectral-Line Survey (VTSS; Dennison et al. 1998). Although both provide higher spatial resolution than WHAM, these imaging surveys provide no spectral information and cannot isolate overlapping emission features. WHAM is also an order of magnitude more sensitive in the survey-mode presented here due to its large beam (1°) sampling and its ability to spectrally remove all contamination from atmospheric sky lines. Here, we present the first multi-wavelength spectral maps of Sh 2-264, an H II region ionized by the O8 III star, λ Ori A (HD 36861; $\ell = 195\overset{\circ}{.}05$, $b = -12\overset{\circ}{.}00$).

Such relatively isolated, large-angle, diffuse H II regions form an important observational bridge between the concentrated, classical, bright nebulae in high-density star-forming environments and the wide-spread, low-density WIM. Unlike the WIM, these regions have simple, well-understood sources of ionization with density characteristics more typical of the diffuse ISM. A few of these have also become important calibration targets for WHAM as regions of moderate intensity over large-angular scales that are visible from its former northern and new southern locations.

λ Ori A anchors a small knot of massive stars in the center of the H II region but dominates the ionizing luminosity of the association. Studies of the recent and on-going star formation in the immediate surroundings of λ Ori suggest that violent stellar activity has reorganized the gas since its formation. A comprehensive review of the region, with particular emphasis on the star-formation history, is presented by Mathieu (2008). For our study, we adopt the hypothesis put forth in Dolan & Mathieu (2001, 2002) that at least one supernova has reorganized the molecular gas in the region 1–2 Myr ago, truncating star formation in the central region near λ Ori and creating the low-density cavity for the diffuse H II region. We also adopt the main-sequence fitting distance for the cluster of 450 ± 50 pc as derived by Dolan & Mathieu (2001) as the distance to the center of Sh 2-264, placing it about 94 pc away from the Galactic Plane. Although the H II region appears to be relatively isolated and dominated predominantly by the influence from λ Ori alone, Sh 2-264 is in the vicinity of the impressive Orion-Eridanus superbubble complex and likely shares a complex, common history with the region. Ochsendorf et al. (2015) present a recent, comprehensive view derived from several multiwavelength surveys.

Using WHAM observations of the Hα line (λ6563) and the faint optical emission lines [S II] λ6716 and [N II] λ6583, we begin a study of the physical state of the diffuse H II region surrounding λ Ori. Hα survey data are combined with [S II] and [N II] observations to learn about the ionization state of the gas and to derive non-thermal velocity and temperature throughout the $\sim$ 62-pc-diameter H II region. Our multiwavelength study also probes into regions beyond the apparent Strömgren sphere, revealing nearby filamentary structure, including a portion of Barnard's Loop (Sh 2-276).

2. OBSERVATIONS

The WHAM spectrometer was designed to detect optical emission lines from diffuse sources at high spectral resolution. The recombination line Hα—typically the brightest of these—is used as the primary tracer to map ionized gas. The physical conditions and ionization state of the gas can then be studied by adding observations of collisionally excited diagnostic lines. WHAM's first major effort produced the first kinematic map of the northern sky ($\delta \geq -30°$) in Hα, which took approximately two years. This map reveals detailed structure of supernova remnants in the form of giant bubbles and super-shells as well as filaments of warm pervasive gas seen far from classical H II regions. The WHAM Northern Sky Survey (WHAM-NSS; Haffner et al. 2003), containing more than 37,500 individual Hα spectra obtained with a 1°diameter beam, is the first spectral survey to map the spatial distribution and kinematic structure of diffuse ionized gas throughout the Galaxy (Reynolds et al. 2002; Haffner et al. 2003). By using a Fabry-Perot spectrometer, WHAM can accept this large solid angle while delivering high spectral resolution ($R \approx 25,000$). This beam size combined with our ability to cleanly separate Galactic and atmospheric emission allows the deepest WHAM observations to be roughly 100 times more sensitive to diffuse, extended emission than current imaging instruments, opening up new opportunities for exploration. It is now located in Chile and has observed the southern sky to provide the first all-sky, kinematic Hα map analogous to surveys of H I in 21 cm. Considerable detail about WHAM's optical design, performance, and data reduction can be found in Tufte (1997) and Haffner et al. (1999).

In this study, Hα observations have been extracted from the WHAM-NSS and have been supplemented with WHAM observations in [S II] and [N II] within a $20° \times 24°$ area surrounding λ Ori. The area surveyed spans the region in Galactic coordinates $\ell = 185°$ to $\ell = 205°$ and $b = -24°$ to $b = -1°$. The Hα observations were mainly taken in 1997 during the northern Hα survey while the [S II] and [N II] observations were obtained in 2006. On-sky exposure times are 30 s for Hα and 60 s for [S II] and [N II] observations. Since the WHAM spectrometer records only spectral information, each observation taken with WHAM represents the average spectrum within a 1°-diameter beam on the sky. The region of study includes 552 original observations in each spectral line. Five directions contain too much

spectral contamination from bright stars having $V < 3$ mag (α, γ, ϵ, and δ Ori; ζ Tau) and are excluded from the final dataset of 547 spectra in each line.

Due to heavy dilution by the one-degree beam relative to diffuse emission, only the brightest stars impact our observations. However, all spectra obtained with WHAM contain noticeable features from the earth's atmosphere. In Hα, the geocoronal Hα emission line is the primary contaminant, which arises from neutral hydrogen being excited by scattered solar Lyβ radiation in the exosphere (Mierkiewicz et al. 2006; Nossal et al. 2006). [S II] observations contain emission from the terrestrial neon line (Ne I λ6717), which originates from city lights scattered into the night sky around Kitt Peak (Reynolds & Ogden 1982; Haffner et al. 1999). This line is located +26.8 km s^{-1} from the geocentric zero of [S II] emission but is much fainter than geocoronal Hα. Since these lines vary independently from the fainter atmospheric lines described below, a Gaussian profile is fit to them and subtracted from each observation. Haffner et al. (2003) describes this procedure for Hα in more depth.

[S II] and [N II] emission—as well as Hα—are also contaminated by $\sim$ 5–7 other atmospheric lines which have full-width-at-half-maximum (FWHM) $\sim$ 10 km s^{-1} and intensities $I \sim 0.05$–0.5 R. The absolute strengths of the atmospheric lines are observed to vary with position and time. Within a given night, these intensities correlate well with zenith distance. Yet the relative strengths of these faint lines are constant to $\sim$ 10%. As a result, we can construct an atmospheric template by observing directions with little Galactic emission multiple times over several nights (Hausen et al. 2002). We use high signal-to-noise averaged spectrum from each observational "block" (up to a 7×7 grid of individual 1°-observations) to determine the absolute intensity level of the template for that block. Semi-automated software is then used to fit Gaussian profiles to multiple Galactic components and remove atmospheric emission present in each individual spectrum. Haffner et al. (2003) describe this procedure in more detail for the Hα survey. For all three spectral windows presented here, the *total* emission from faint atmospheric lines in our 200 km s^{-1} spectral window near $v_{\rm LSR} = 0$ km s^{-1} varies from about 0.2 to 0.8 R depending on the night and look direction. We are able to determine the absolute intensity level of the atmospheric templates better than 10% in most spectra. Directions where the Galactic emission is very bright (> 20 R) make this determination difficult, but for the same reason any residual contamination from atmospheric lines also becomes negligible. From our analysis, we estimate a conservative systematic uncertainty of 0.05 R contributed by residuals over the whole 200 km s^{-1} spectrum.

Each spectrum is calibrated to obtain a stable velocity zero-point with respect to the local standard of rest (LSR). Velocity calibration in Hα and [S II] is accomplished by using the brighter atmospheric lines (geocoronal Hα and terrestrial Ne I). Line centers fit during atmospheric subtraction are recorded and used to establish the geocentric velocity frame (e.g., Haffner et al. 1999, 2003). Translation from the geocentric frame to LSR is calculated using the same traditional value for the Standard Solar Motion adopted by 21 cm observers, +20 km s^{-1} toward $\alpha_{1900} = 18^h0, \delta_{1900} = +30\overset{\circ}{.}0$ (Haffner et al. 2003). A thorium argon (Th-Ar) lamp is used as the wavelength calibrator for the [N II] observations. Velocity calibration can also be verified for the [N II] observations by comparing Hα and [N II] spectra from bright nebulae—with the assumption that the emission from both lines takes on relatively similar velocity profiles (Haffner et al. 1999).

Our intensity calibration is tied to regular observations of NGC 7000 (North American Nebula; NAN), a large emission nebula in Cygnus. NGC 7000 subtends a large enough solid angle to fill WHAM's 1°-beam and bright enough to achieve very high signal-to-noise in our typical exposure times. We use the absolute Hα intensity of NGC 7000 as determined by Scherb (1981) who used the planetary nebula NGC 7662 and standard stars as reference objects. This study measured the intensity of the NGC 7000 to be 850 ± 50 R for a 49′ FOV using a Fabry-Perot spectrometer. [S II] and [N II] emission is calibrated by applying a correction factor of 0.94 for [S II] and 1.15 for [N II]. These factors account for instrument throughput differences between these lines and Hα throughout the instrument (Haffner et al. 1999).

3. RESULTS AND DISCUSSION

Figures 1a, 1b, and 1c display intensity-integrated maps of Hα, [N II], and [S II] emission surrounding λ Ori as sampled in the WHAM survey mode. Each map is constructed from 547 individual 1°-beam observations. The color represents the intensity of each emission spectrum integrated over velocities $v_{\rm LSR} = -80$ to +80 km s^{-1} after subtraction of atmospheric and continuum emission as discussed in §2. These three intensity maps look qualitatively similar with the brightest emission around λ Ori at $(\ell, b) = (195\overset{\circ}{.}05, -11\overset{\circ}{.}99)$ revealing the 8°-diameter Strömgren sphere. Darker regions still contain emission from the WIM but are much fainter than the λ Ori H II region.

Figures 1d, 1e, and 1f show several line-ratio combinations: [S II]/[N II], [N II]/Hα, and [S II]/Hα. These reveal that the H II region has distinct spectral properties compared to the more diffuse surrounding emission—in addition to its elevated optical line intensities. The spatial distribution depicted in these maps complements the quantitative

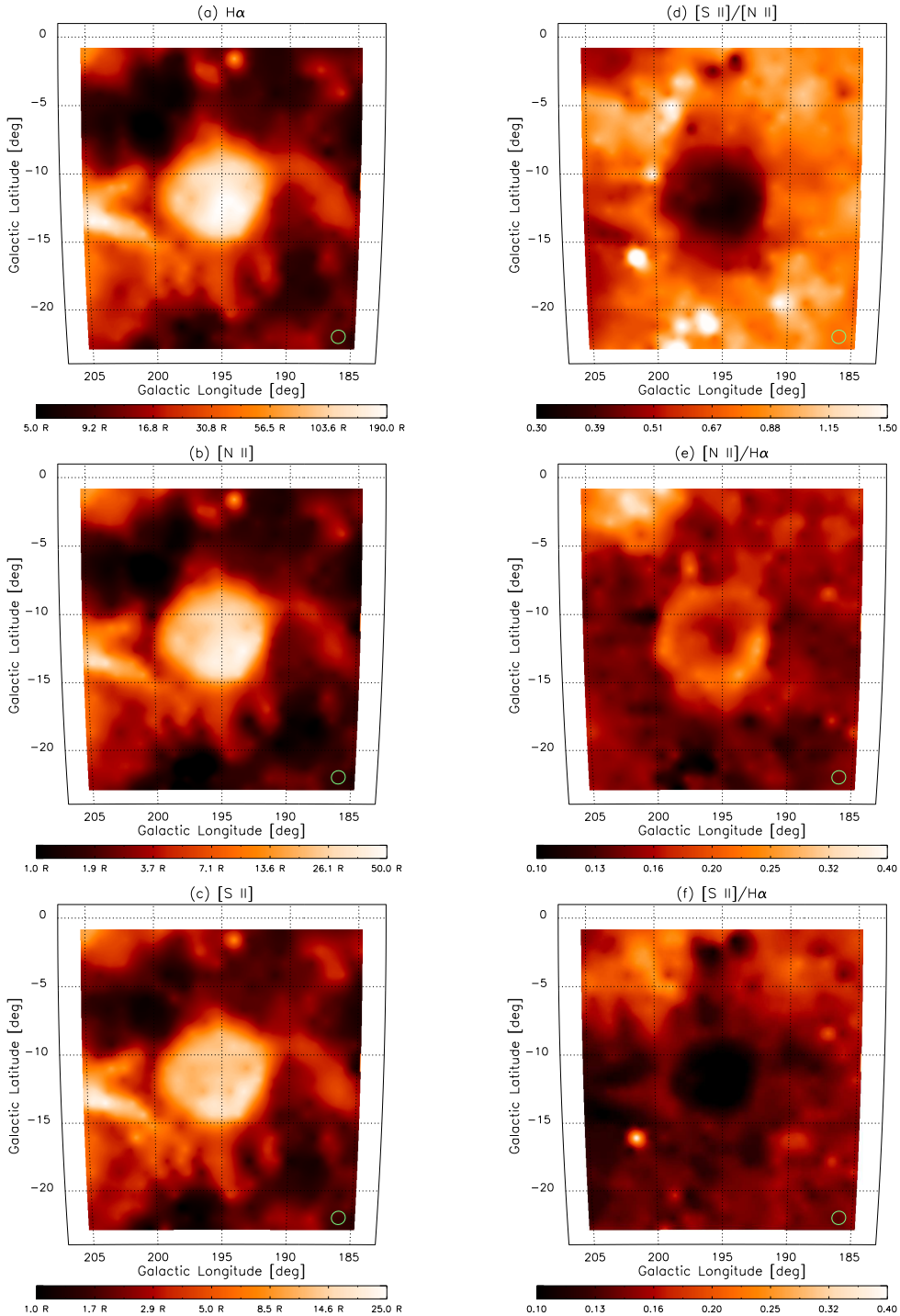

Figure 1. Smoothly interpolated *a*) Hα, (*b*) [N II], and (*c*) [S II] emission-line maps and (*d*) [S II]/[N II], (*e*) [N II]/Hα, and (*f*) [S II]/Hα line-ratio maps of the ionized region surrounding λ Ori ($\ell = 195\overset{\circ}{.}05,\ b = -12\overset{\circ}{.}00$) as surveyed by WHAM. Intensity is integrated over velocities between $v_{\rm LSR} = -80$ km s^{-1} and +80 km s^{-1} for each of the 547 individual spectra. Emission-line maps are logarithmically scaled and line-ratio maps are linearly scaled between the range denoted on the colorbar under each map. A circle in the bottom-right of each figure depicts the size of the WHAM beam on the sky. Axes are degrees of Galactic longitude and latitude.

analysis in sections below that derive physical conditions of the gas surrounding λ Ori.

Figure 2 shows a pair of sample individual spectra in each of the three lines along two different lines of sight in the region. The spectra highlighted in Figure 2 are toward the brightest direction of the H II region at ($\ell,\ b$) = ($195\overset{\circ}{.}40,\ -12\overset{\circ}{.}73$) and one $\sim 8^\circ$ away at ($\ell,\ b$) = ($201\overset{\circ}{.}33,\ -6\overset{\circ}{.}79$). The spectra are plotted as intensity (R/(km s^{-1}))

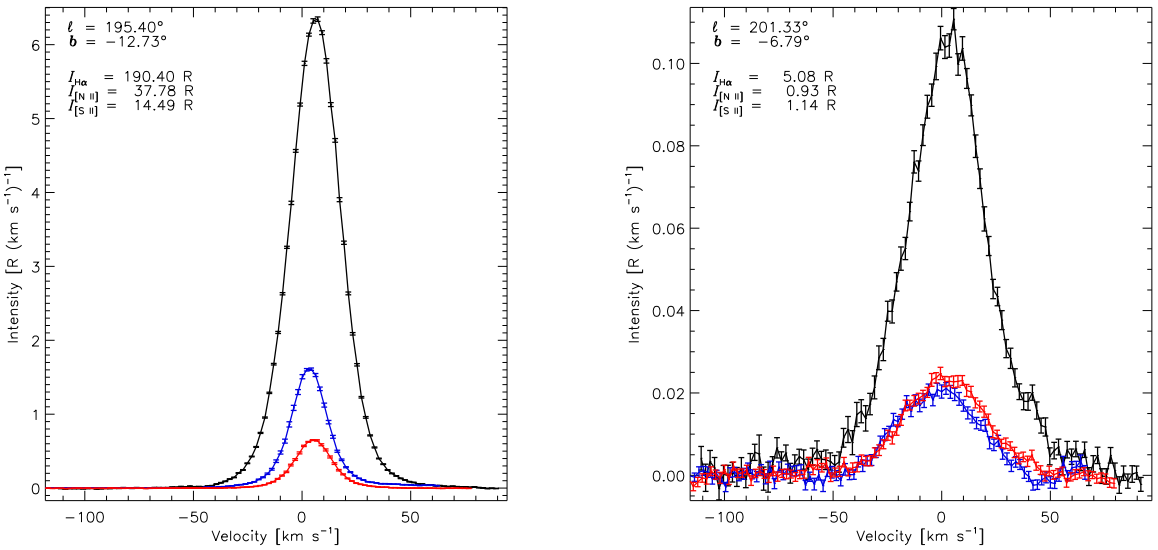

Figure 2. Sample Hα (*black*), [N II] (*blue*), and [S II] (*red*) spectra from two directions, (ℓ, b) = (195.°4, −12.°73) and (201.°33, −6.°79), are plotted as intensity vs. LSR velocity. Total integrated intensities for each line are noted in the upper left corner of each plot. These two examples are selected from the 547 observations used to create the maps in Figure 1.

versus LSR velocity (km s^{-1}). The total integrated intensity of the emission lines is labeled in the upper left corner of each plot. Note that the intensity of [S II] and [N II] increases relative to Hα in fainter regions, as can also be seen in Figures 1e and 1f. In sections below, we often concentrate on the H II region—observations within 4° of λ Ori. These bright spectra are dominated by the nebular emission and are fit well by a single Gaussian. This region of focus spans roughly $\ell = 190°$ to 200° and $b = -17°$ to $-7°$.

Table 1 summarizes several basic properties for a line of sight centered near λ Ori. We adopt the selective extinction parameter, $E(B-V)$, from photometry and intrinsic colors presented in Cruz-González et al. (1974); spectral type from Maìz-Appellaniz et al. (2004); and distance from Dolan & Mathieu (2001). Using this distance, we calculate the distance away from the Galactic mid-plane, $z = d \sin b$, where d is the distance to λ Ori, and b is the Galactic latitude. Beams with elevated Hα extend to approximately $\theta_{HII} \sim 4°$, which then leads to an estimate of the physical radius of the H II region, R_{HII}. The values for L_c and n_e are computed below in §3.1. Uncertainties on these last three parameters are dominated by the uncertainty in the distance to λ Ori.

3.1. *Hα EMISSION*

From Haffner et al. (2003),

$$EM \equiv \int n_e^2 \, dl = 2.75 \; T_4^{0.9} \; I_{H\alpha} \; (\mathrm{cm}^{-6} \; \mathrm{pc}) \tag{1}$$

where $I_{\mathrm{H}\alpha}$ is measured in Rayleighs. Including a correction for dust extinction and assuming a temperature of 8000 K, we arrive at this standard equation from Reynolds & Ogden (1982):

$$\mathrm{EM} = 2.25 \; I_{\mathrm{H}\alpha} \; e^{2.75 \; E(B-V)} \; (\mathrm{cm}^{-6} \; \mathrm{pc}). \tag{2}$$

For simplicity we assume the selective extinction, $E(B-V)$, is the same throughout the H II region as measured toward λ Ori. Future work will incorporate Hβ observations to correct $I_{\mathrm{H}\alpha}$ for each WHAM beam. The peak Hα intensity ($I_{\mathrm{H}\alpha}$) is measured to be 185 R. From equation (1), we see that $I_{\mathrm{H}\alpha} \propto \mathrm{EM} = \int n_e^2 dl$, and thus the ionization of the nebula. By summing over the total observed intensity of the H II region, we can estimate the luminosity of the Lyman continuum photons (L_c) produced by λ Ori using the following equation (from Haffner 2001):

$$L_c = \frac{4\pi d^2}{\epsilon} \int I_{\mathrm{H}\alpha} \; e^{\tau_{H\alpha}} \, d\Omega \; (\mathrm{ph \; s}^{-1}), \tag{3}$$

where d is the distance to the region, $I_{\mathrm{H}\alpha}$ is the Hα intensity emitted over the solid angle $d\Omega$, and $e^{\tau_{H\alpha}}$ is the extinction correction, defined observationally with $e^{2.75 \; E(B-V)}$. The factor 2.75 is computed from the extinction models of Cardelli et al. (1989) at Hα assuming the typical diffuse total to selective extinction (R_v) ratio of 3.1. ϵ is

Table 1. Selected Parameters of λ Ori A and Sharpless 2-264.

Parameter	Symbol	Value
Star		HD 36861
Spectral type		O8 III
Galactic coordinates	(ℓ, b)	(195.°05, -12.°00)
Selective extinction	$E(B-V)$	0.12
Distance from Sun	d	450 ± 50 pc
Distance from Galactic Plane	z	-94 ± 10 pc
Angular radius of H II region	θ_{HII}	4°
Physical radius of H II region	R_{HII}	31 ± 3 pc
Hα intensity[a]	$I_{\rm H\alpha}$	185 ± 1 R
Emission measure[a]	EM	579 ± 3 cm^{-6} pc
Ionizing photon luminosity[b]	L_c	$(7.2^{+1.5}_{-1.7}) \times 10^{48}$ ph s^{-1}
Average H II region density[b]	n_e	2.5 ± 0.3 cm^{-3}

[a] As sampled by the one-degree WHAM beam toward λ Ori. Higher intensity emission may exist on smaller scales.

[b] As derived in this work. See §3.1

the fraction of Hα photons produced per Lyman continuum photon, 0.47 for gas at 8000 K (Martin 1988). We compute the Hα intensity of the H II region using $I_{\rm H\alpha} = (I_{\rm H\alpha,obs} - I_{\rm H\alpha,bf})$. Here, $I_{\rm H\alpha,obs}$ is the observed, integrated intensity ($v_{\rm LSR} = -80$ to $+80$ km s^{-1}) of each spectrum, and $I_{\rm H\alpha,bf}$ is the intensity along the line of sight from behind and in front of the H II region. Examining the distribution of intensities in this region by taking cuts through Sh 2-264, we estimate the average background/foreground emission $I_{\rm H\alpha,bf} = 10$ R.

Approximating the integral in equation (3) as a sum over WHAM beams,

$$L_c = 2.03 \times 10^{43} d^2 \left(\frac{\Omega_{HII}}{N\Omega_p}\right) \sum_N (I_{\rm H\alpha,obs} - I_{\rm H\alpha,bf})\ e^{2.75\ E(B-V)}\ \Omega_p\ ({\rm ph\ s^{-1}}). \quad (4)$$

Here, Ω_p represents the solid angle subtended by a single pointing in the 1°-circular beam of WHAM (2.39×10^{-4} sr); $\Omega_{HII}/(N\Omega_p)$ is a correction factor that estimates gaps and overlaps of the survey grid within the H II region; and N is the number of observations within a 4°-radius region surrounding λ Ori. For a circular region on the sky (i.e., cone in solid angle),

$$\Omega_{HII} = 2\pi(1 - \cos(4^\circ)) = 1.53 \times 10^{-2}\ ({\rm sr}) \quad (5)$$

and

$$\Omega_{HII}/N\Omega_p = (1.53 \times 10^{-2}\ {\rm sr})/(60 \times 2.39 \times 10^{-4}\ {\rm sr}) = 1.07. \quad (6)$$

Using the $E(B-V)$ and distance in Table 1, we find $L_c = (7.2^{+1.5}_{-1.7}) \times 10^{48}$ ph s^{-1}. The uncertainty on this value is dominated by the uncertainty of the distance to λ Ori resulting in a $\sim 20\%$ on our estimate of L_c. Our calculation of L_c is low compared to recent model calculations for O8 III stars, $\sim 1.7 \times 10^{49}$ ph s^{-1} (e.g., Vacca et al. 1996). However—assuming the model reflects the true output of the star—our estimate using the Hα intensity of the H II region is expected to be a lower limit if any ionizing flux escapes the region. Our correction for Hα removed from our line of sight by dust scattering ($e^{\tau_{H\alpha}}$) using the selective extinction toward λ Ori assumes the value is constant across the nebula. We have no specific reason to expect this correction to be too low on average, but future work using Hβ will remove this assumption.

With L_c, we can also estimate the density (n_e) of the emitting gas. In a spherical H II region where H in the nebula is assumed to be fully ionized and n_e constant, the recombination balance equation is:

$$L_c = \alpha_B n_e^2 \frac{4\pi}{3} R_{HII}^3 \quad (7)$$

where, α_B is the recombination coefficient and equals to 3.10×10^{13} cm^3 s^{-1} for gas at $T \sim 8000$ K (Osterbrock 1989).

Then,

$$n_e = 162 \sqrt{\frac{L_{c48}}{R_{HII}^3}} \ (\mathrm{cm}^{-3}) \tag{8}$$

In this equation, L_{c48} is in units of 10^{48} ph s^{-1}, R_{HII} is in pc, and n_e is in cm^{-3}. With R$_{HII}$ = 31 ± 3 pc and $L_{c48} = 7.2^{+1.5}_{-1.7}$ we find $n_e = 2.5 \pm 0.3$ cm^{-3}.

3.2. *[S II] AND [N II] LINE RATIOS*

The relative intensities of metal-line emission to Hα and each other can reveal information about the ionization state and temperature of diffuse ionized gas (e.g., Haffner et al. 1999; Reynolds et al. 1999; Madsen et al. 2006). We use the Hα, [S II], and [N II] intensity maps shown in Figure 1 to examine [N II]/Hα, [S II]/Hα, and [S II]/[N II] emission line ratio behavior. The Hα intensity decreases by a factor of approximately 19 from the center to the edge of the H II region (with our one-degree beam sampling), from $I_{\mathrm{H}\alpha} \sim 190$ R near the center to $I_{\mathrm{H}\alpha} \sim 10$ R on the periphery of the area under analysis. However, line ratios vary by much less. The [S II]/Hα ratio increases from ~ 0.1 at the center to ~ 0.2 at the edge, and the [N II]/Hα ratio increases from ~ 0.2 at the center to ~ 0.35 at the edge of the nebula, factors of 2 and 1.75 from the center to the edge of the nebula, respectively. The [S II]/[N II] ratio also increases by about a factor of 2.5 from ~ 0.4 at the center to ~ 1 at the edge. The range of in the [S II]/Hα, [N II]/Hα, and [S II]/[N II] line ratios for this diffuse nebula are not too different from those seen in the WIM (e.g., Madsen et al. 2006), but the trends show different behaviors.

Past studies of diffuse Hα, [S II], and [N II] and more recent investigations of the WIM carried out with WHAM show that there is a good correlation between the line ratios and variation in the temperature of the WIM (Reynolds 1985a, 1988; Haffner et al. 1999; Reynolds et al. 1999). Haffner et al. (1999) suggested that the tight correlation of [S II]/[N II] seen in their data arose simply from the dominance of S^+ and N^+ ionization states in this gas together with similar excitation energy of these two emission lines. They derived estimates of the electron temperature and ionization state of sulfur for a large region of the sky. While all their assumptions for the WIM are not valid in a classical H II region since the ionization structure of emission nebulae changes significantly over smaller scales, the techniques used to examine the line ratio behavior are still useful here.

The basic equation for the intensity of emission lines from collisionally excited ions found in Osterbrock (1989) and Haffner et al. (1999) is given as:

$$I_\nu = \frac{f_\nu}{4\pi} \int n_i n_e \frac{8.63 \times 10^{-6}}{T^{0.5}} \frac{\Omega(i,j)}{w_i} e^{(E_{i,j}/kT)} dl \tag{9}$$

where I_ν is in units of ph s^{-1} cm^{-2} sr^{-1}, $\Omega(i,j)$ is the collision strength of the transition, w_i is the statistical weight of the ground level, E_{ij} is the energy of the upper level of the transition above the lower, n_i and n_e is the ion and electron density, respectively, k is Boltzmann's constant, T is the temperature of the gas, dl is the pathlength through the emitting region, and f_ν is the fraction of downward transitions that produce the emission line in question (e.g., Osterbrock 1989; Haffner et al. 1999).

The intensities of [S II] λ6716 and [N II] λ6583 emission are then:

$$I_{6716}(R) = 2.79 \times 10^5 \left(\frac{H^+}{H}\right)^{-1} \left(\frac{S}{H}\right) \left(\frac{S^+}{S}\right) T_4^{-0.593} \, e^{-2.14/T_4} \ \mathrm{EM}, \tag{10}$$

and

$$I_{6583}(R) = 5.95 \times 10^4 \left(\frac{H^+}{H}\right)^{-1} \left(\frac{N}{H}\right) \left(\frac{N^+}{N}\right) T_4^{-0.474} \, e^{-2.18/T_4} \ \mathrm{EM}, \tag{11}$$

where T_4 is in units of 10^4 K and EM is related to $I_{\mathrm{H}\alpha}$ in equation (1). The ratio of the metal emission lines is then:

$$\frac{I_{6716}}{I_{6583}} = 4.69 \frac{(\frac{S}{H})}{(\frac{N}{H})} \frac{(\frac{S^+}{S})}{(\frac{N^+}{N})} T_4^{-0.119} \, e^{0.04/T_4}. \tag{12}$$

Haffner et al. (1999) adopted parameters for (S/H)= 1.86×10^{-5} from Anders and Grevesse (1989) and (N/H)= 7.5×10^{-5} from Meyer et al. (1997) for the gas-phase abundances of S and N. This ratio is insensitive to temperature because of the nearly identical energies required to excite the lines. As a result, when [S II]/[N II] is seen to be constant throughout a spatial region, $(S^+/S)/(N^+/N)$ also changes little.

Models (Sokolowski 1994; Sembach et al. 2000) have shown in diffusely ionized regions (e.g., the WIM, IVCs, HVCs, etc.) N^+/N^0 tracks H^+/H^0 because of their similar first ionization potentials (14.5 eV and 13.6 eV, respectively) and a weak charge-exchange reaction. This relationship allows us to use equation (11) as a rough estimate of the electron temperature within the emitting gas. Furthermore, in these regions where the fractional ionization of H has been also measured to be near unity (Reynolds et al. 1998; Madsen et al. 2006) and higher ionization species such as He^+ and O^{++} are extremely faint or not detected (Reynolds & Tufte 1995; Tufte 1997; Howk & Savage 1999; Madsen et al. 2006), N^+ should be the dominant ion state with $N^+ \sim 0.8 - 1.0$ (Haffner et al. 1999). On the other hand, S has a second ionization potential of 23.4 eV, just below neutral He at 24.6 eV. As a result, it is likely partially ionized to S^{++}. Using this justification and equation (12), Haffner et al. (1999) estimated ionization states of S^+/S that range between about 0.25 and 0.8 in the WIM, with an average in the local diffuse background of 0.6 – 0.65. Such ratios have been found to be systematically higher in the WIM than in classical H II regions (e.g., Reynolds 1988; Reynolds et al. 1999; Haffner et al. 1999). The lower S^+/S ratios in H II regions is somewhat expected since the ionization parameter (n_{ph}/n_e) is large and S^+ is ionized to S^{++} more readily, which produces a corresponding decrease in the observed [S II] intensity relative to Hα (Domgörgen & Mathis 1994; Sokolowski 1994; Haffner et al. 1999). However, Haffner et al. (1999) show that a higher electron temperature (T_e) in the WIM will also increase the [S II]/Hα ratio.

Figure 3 shows the behavior of [S II]/Hα, [N II]/Hα and [S II]/[N II] as a function of Hα intensity as well as [S II]/Hα vs. [N II]/Hα throughout this region containing Sh 2-264. The core of the H II region, observations within 4° of λ Ori, are highlighted in red. In general, Figure 3a shows a marked increase in [S II]/Hα ratio with decreasing Hα intensity, both inside and outside the H II region. A trend in the [N II]/Hα ratio in Figure 3b is less pronounced, although the H II region has a distinctly elevated track in this ratio, which is visible as the radial gradient close to the star in Figure 1e. As equation (12) shows, Figure 3c ([S II]/[N II] vs. Hα) is fairly insensitive to temperature so that variation is dominated by the ion ratio (S^+/N^+). Figure 3d plots [S II]/Hα and [N II]/Hα against one other, with the H II region again occupying a distinct area of the figure. The distinct separation of H II regions from the more diffuse background is common in these studies (*e.g.*, Figures 7 & 13 of Madsen et al. 2006) and highlights the different natures of the radiation field near ionizing sources and out in the diffusely ionized and more widely distributed ISM.

3.3. *LINE WIDTHS*

We can use the widths (FWHM) of Hα and [S II] emission lines to measure temperature and nonthermal velocity throughout the λ Ori H II region. This method was utilized by Reynolds (1985a) to show that the properties of diffuse gas along several lines of sights in the WIM differs from those in classical H II regions. The temperature and nonthermal velocity of the emitting gas in Sh 2-264 can be derived from the total line widths of [S II] and Hα, if the emission lines originate from ions that are uniformly mixed within the H II region (Reynolds 1985b, 1988).

Some evidence that the ions share a kinematic profile is provided by Figure 2 above, which shows the agreement in the shape and extent of the line profiles of [S II] and Hα emission. Further confidence comes from comparing some of the quantitative properties of the line emissions. In Figure 4, we plot the intensity of the Hα emission against the intensity of corresponding [S II] emission. This figure reveals that the [S II] is generally correlated with Hα (deviations are highlighted in the [S II]/Hα ratio plot of Figure 3a). Furthermore, the peak of these lines track each other in radial velocity as seen in Figure 5. The correlation in the plots of Figures 4 and 5 as well as the similarity in shape of the line profiles in Figure 2 provide sufficient evidence that components within the two lines originate from the same region of gas for the purpose of our analysis. However, our ability to accurately derive the widths decreases when the H II region component becomes comparable to the foreground and/or background emission in this complex area of the Galaxy. For the rest of this analysis, we use only the observations within a 4°-radius of λ Ori where we are able to isolate the H II region emission.

The Hα and [S II] total line widths (FWHM), W_H and W_S, are given by:

$$W_H \approx 21.4 \left[\frac{T_i}{10^4} + \left(\frac{v}{12.8} \right)^2 + 0.070 \right]^{1/2} \text{(km s}^{-1}\text{)} \tag{13}$$

and

$$W_S \approx 3.78 \left[\frac{T_i}{10^4} + \left(\frac{v}{2.27} \right)^2 \right]^{1/2} \text{(km s}^{-1}\text{)} \tag{14}$$

where T_i is temperature as measured by the ion speeds and v is the most probable speed of the nonthermal velocity distribution; the extra 0.070 term in equation (13) accounts for width due to the fine structure of the Hα line (Reynolds 1985a). It is reasonable to treat the nonthermal radial velocity distribution as a Gaussian because the [S II] components,

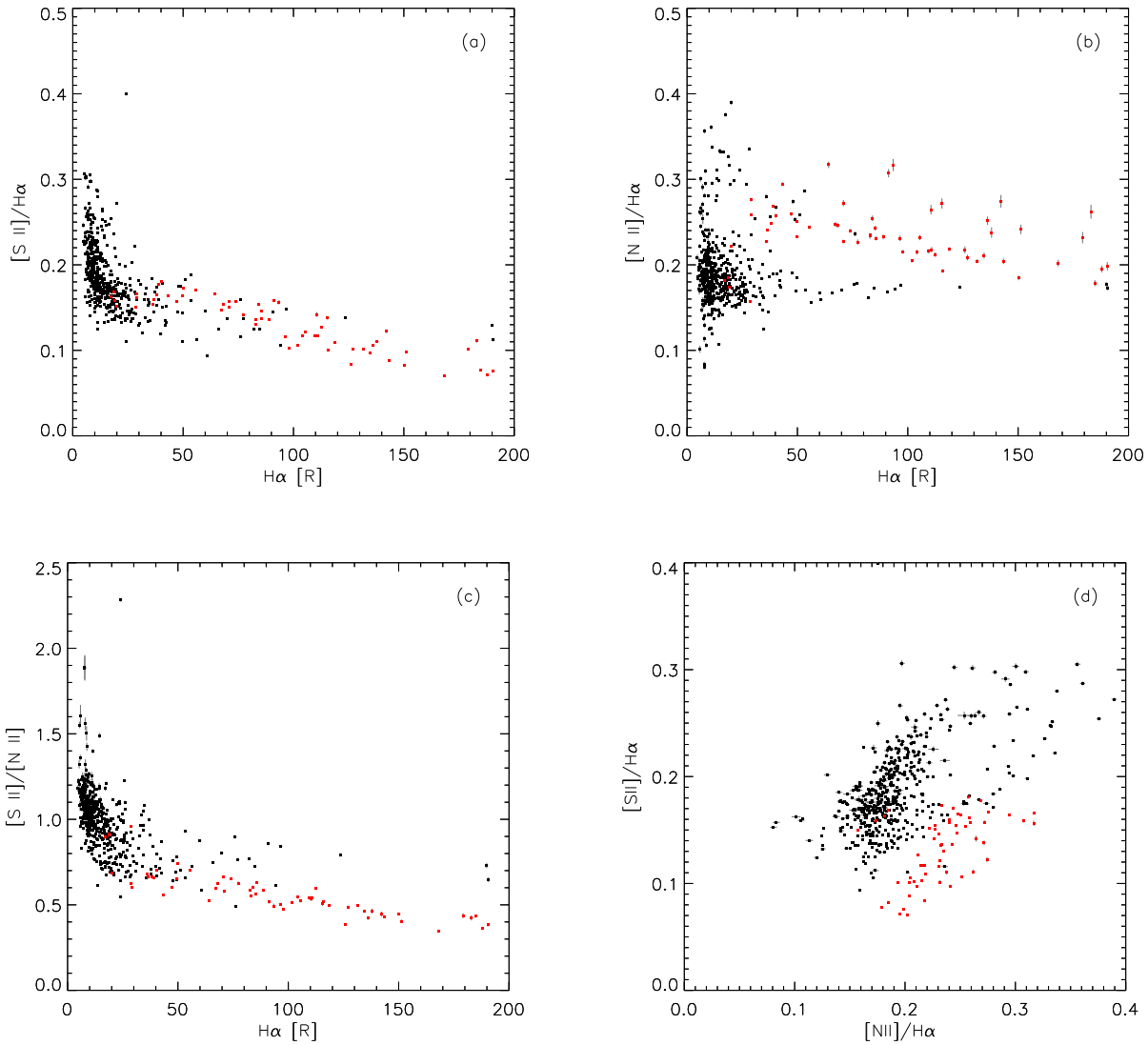

Figure 3. (*a*) [S II]/Hα vs. Hα, (*b*) [N II]/Hα vs. Hα, (*c*) [S II]/[N II] vs. Hα, and (*d*) [S II]/Hα vs. [N II]/Hα relationships for pointings in Figure 1 around λ Ori. Intensities are integrated between $v_{\rm LSR} = -80$ and $+80$ km s^{-1}. Error bars (*gray*) on each symbol represent the uncertainty of the intensity or ratio. Many error bars are smaller than the plotted symbols since uncertainties on integrated intensities are very small for WHAM observations in this moderately bright region of the Galaxy. Data points within 4° of λ Ori are highlighted in red.

whose widths are dominated by nonthermal motions at these temperatures (see equation (14) and the limit on T_i and v) are well-fit by Gaussian profiles.

The mode of the nonthermal velocity distribution, or most probable speed v, and the gas temperature T_i are then given by:

$$v \approx \left[\frac{\left(\frac{W_H}{21.4}\right)^2 - \left(\frac{W_S}{3.78}\right)^2 - 0.70}{\left(\frac{1}{12.8^2} - \frac{1}{2.27^2}\right)} \right]^{1/2} \quad (\mathrm{km\ s^{-1}}) \tag{15}$$

$$T_i \approx 10^4 \left[\left(\frac{W_S}{3.78}\right)^2 - \left(\frac{v}{2.27}\right)^2 \right] = 10^4 \left[\left(\frac{W_H}{21.4}\right)^2 - \left(\frac{v}{12.8}\right)^2 - 0.070 \right] \mathrm{(K)} \tag{16}$$

A grid of the resulting values for T_i and v is superposed onto Figure 6, a plot of the observed widths of Hα and [S II] along lines of sight throughout the H II region. Note that as with Figures 4 and 5, there is general correlation between the widths of the two lines, suggesting that the same underlying physical conditions drive the formation of the

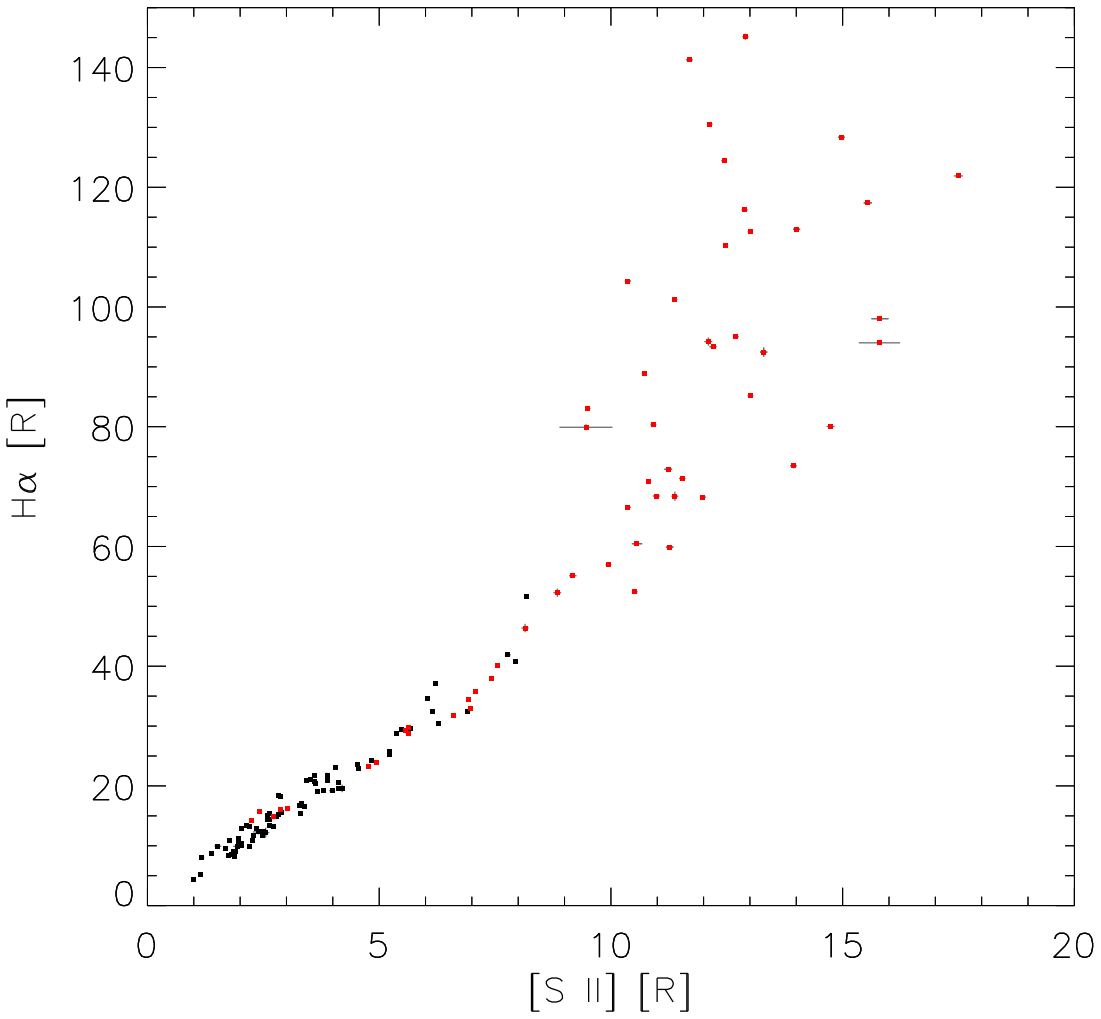

Figure 4. Hα vs. [S II] fitted component areas for observations within 6° of λ Ori, the rough extent of its H II region. Those pointings closer than 4° are highlighted in red. Error bars (*gray*) on each symbol represent a 1σ uncertainty in the fitted Gaussian component area. Note that many error bars are smaller than the plotted symbols since the area (intensity) is very well-determined by WHAM observations in this moderately bright region of the Galaxy. Uncertainties do increase in some directions when spectral profiles become more complex and require several comparable Gaussian components.

line profiles of each element and that the emission arrises from the same region. Although the H II region emission is the dominant component in these spectra within 4°of λ Ori, a few on the edge of the region show noticeable blending with a second component. Examining the ratio of the intensities of the H II region component (I_{HII}) to the secondary component (I_2), we define blended directions as those having $I_2/I_{HII} > 0.25$ in either Hα or [S II]. These directions generally correspond with outliers or points with larger errorbars in Figure 6, which we highlight in purple.

We mapped the spatial trends of these temperature and nonthermal velocity parameters (Figures 7 & 8). Using this analysis, the ion temperature throughout the nebula ranges from about 4000 K to 8000 K, with the higher values in the outer parts of the nebula. Such a trend is not unexpected close to an ionizing source. Near the source of an H II region the ionization rate is high and due to their high interaction cross-section, photons with energy closest to 13.6 eV are used up. Higher energy photons escape to the edge of the H II region and can heat the surrounding gas to higher temperatures. Heiles et al. (2000) derived similar average temperatures for H II region as a whole by comparing radio and Hα emission.

The nonthermal velocity map (Figure 8) reveals a decrease in velocity from about 10 km s^{-1} to 5 km s^{-1} from

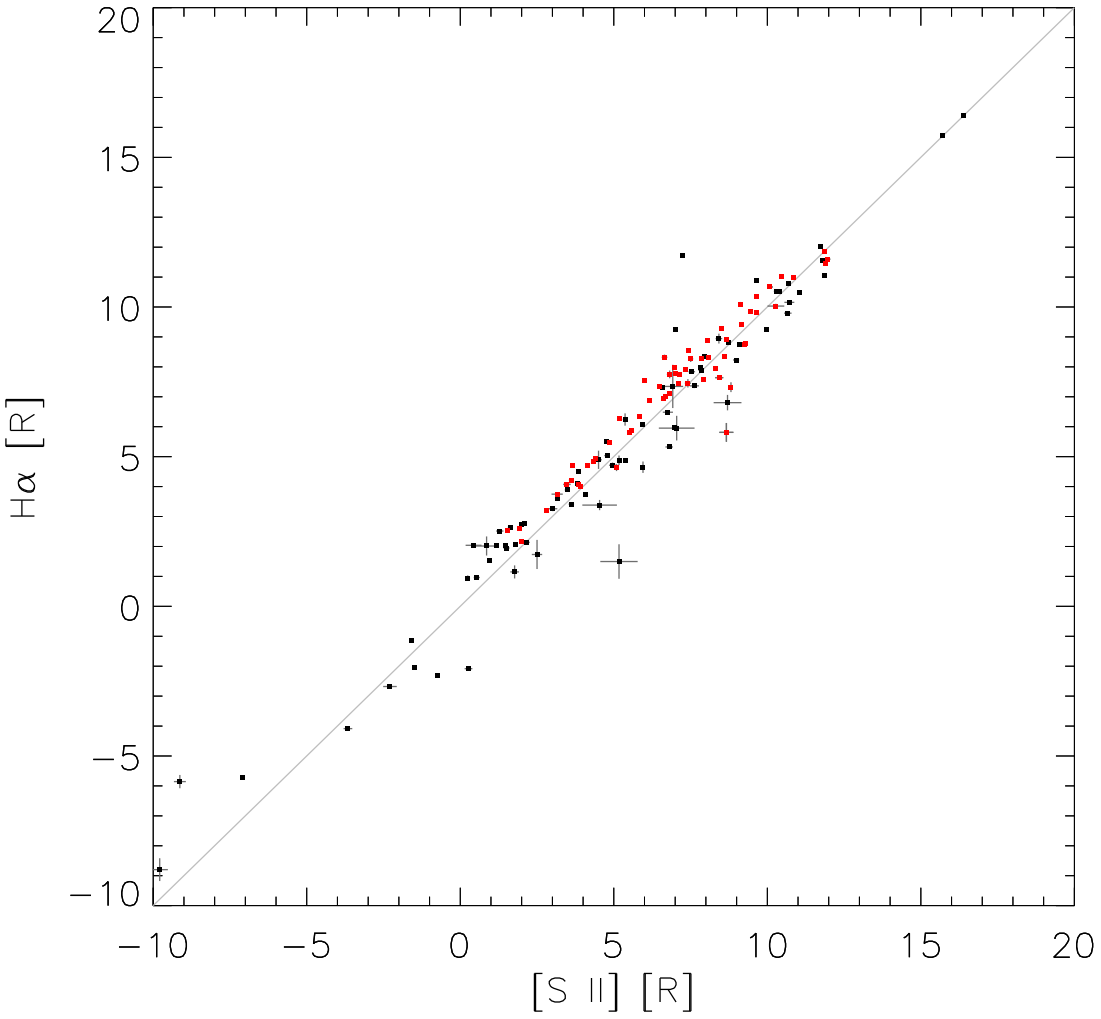

Figure 5. Hα vs. [S II] fitted component means for observations within 6° of λ Ori, the rough extent of its H II region. Those pointings closer than 4° are highlighted in red. Error bars (*gray*) on each symbol represent a 1σ uncertainty in the fitted Gaussian mean. A line of unity (*gray*) is provided for reference.

the center to the edge of the lower half of the map, perhaps revealing the expansion of the H II region. In the upper half, nonthermal velocities are noticeably higher. We note that this area of increased nonthermal component corresponds to the "trunks" of evaporating material that are more prominent in this portion of the nebula (e.g., Figure 5 of Ochsendorf et al. 2015). With WHAM's limited spatial resolution in its survey mode, we can only speculate that ablation and flow from these active regions contributes to a more complex velocity profile. The nonthermal velocities at the edge of our studied region appear to increase. This effect could be caused by emission from the nebula diminishing to an intensity comparable to emission elsewhere along the line of sight (e.g., from the WIM or other diffuse portions of the Orion-Eridanus region). When the line profile is no longer dominated by a single component, these derived values become less valid without more complex procedures to isolate the H II region.

The [N II]/Hα ratio also has the potential to provide an estimate of the electron temperature throughout the nebula. Combining equations (2) and (11), we have:

$$\frac{I_{6583}}{I_{H\alpha}} = 1.63 \times 10^5 \left(\frac{H^+}{H}\right)^{-1} \left(\frac{N}{H}\right) \left(\frac{N^+}{N}\right) T_4^{0.426} e^{-2.18/T_4}, \tag{17}$$

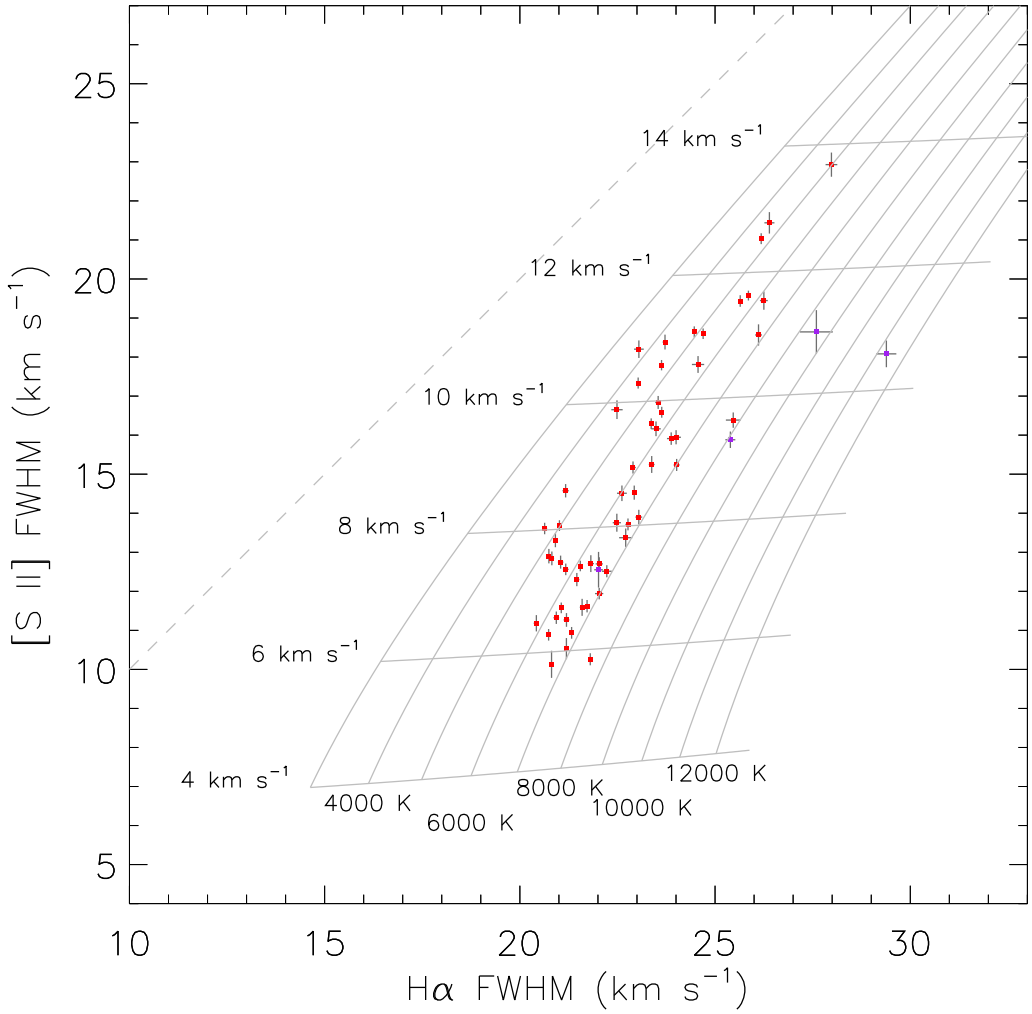

Figure 6. Width (FWHM) of [S II] emission components plotted against the width of their corresponding Hα component. Error bars (*gray*) represent a 1σ uncertainty of the fitted Gaussian widths. The solid, gray grid lines indicate the combination of temperature and nonthermal gas motion that accounts for each pair of [S II] and Hα line widths. The dashed, gray line traces a unity relationship for reference. The data points here are limited to those within 4° of λ Ori where the H II region dominates emission along the line of sight. Observations with significant multiple-component blending are highlighted in purple; parameters determined from the H II region component fit are less certain for these points.

where T_4 is electron temperature in units of 10^4 K and (N/H) is the gas phase abundance of nitrogen. We use the N/H gas-phase abundance of 7.5×10^{-5} from Meyer et al. (1997). Starting with the simplest assumption that $(H^+/H) = 1$ in the H II region, our equation for ratio then becomes:

$$\frac{I_{6583}}{I_{H\alpha}} = 12.2 \left(\frac{N^+}{N}\right) T_4^{0.426}\, e^{-2.18/T_4} \tag{18}$$

Using this equation and the [N II]/Hα line ratio of the H II region emission components, we can derive an electron temperature at each location. Unfortunately, (N^+/N) cannot be determined independently using these observations alone. To provide some basic reference, we use $(N^+/N) = 1$ in Figure 9 to compare the T_e and T_i values from these two different methods. Lowering (N^+/N) moves points to the right in this plot as higher T_e is then required to produce the same [N II] emission. It is clear that applying a single value of (N^+/N) throughout the nebula will not lead to better agreement between the two methods. Although the temperatures do correlate, they span different ranges. For

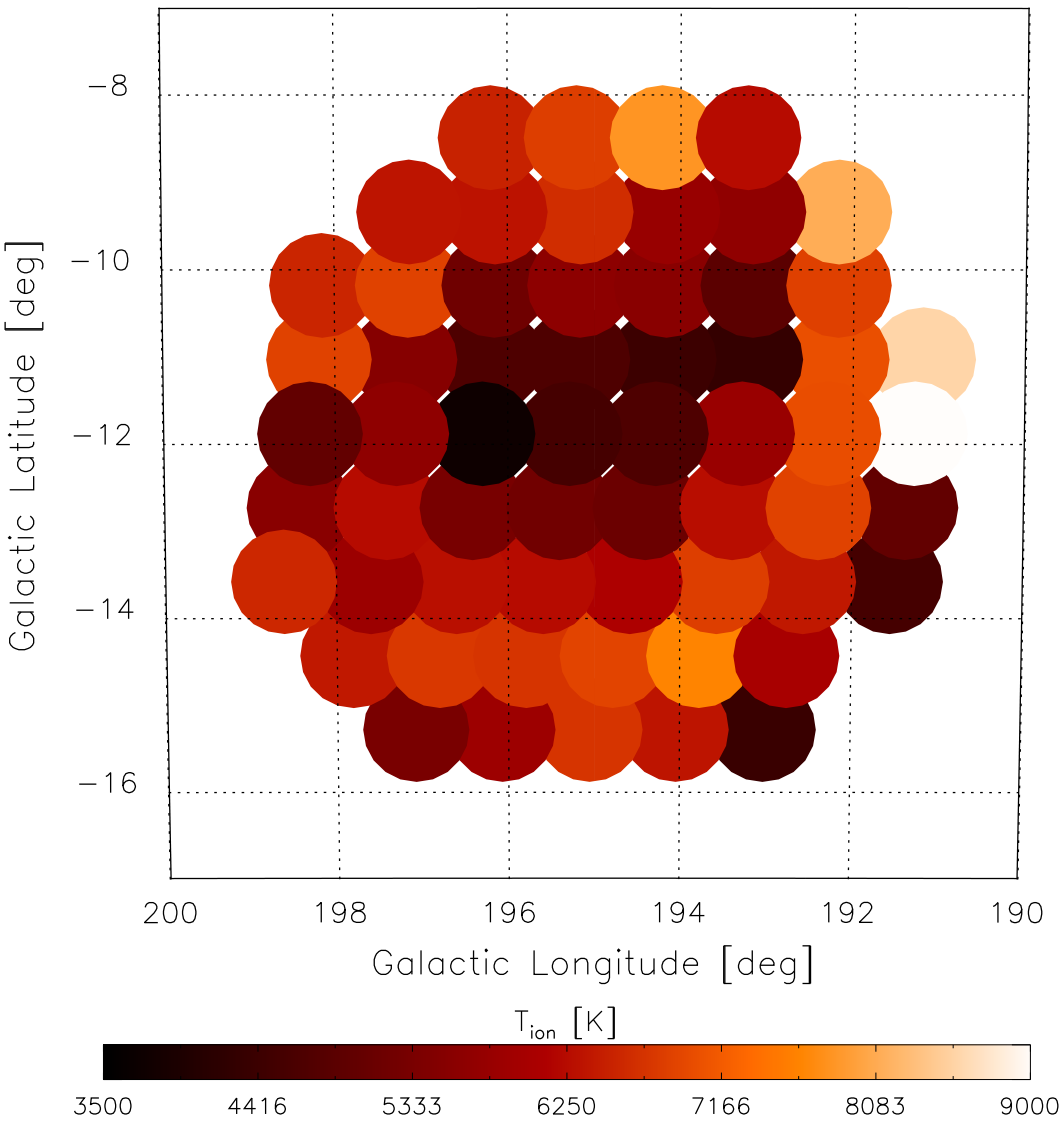

Figure 7. Ion temperature within the λ Ori H II region as derived from the observed [S II] and Hα component widths. Temperatures are depicted as filled circles that show the coverage and sampling of the WHAM 1°-beam throughout a region within 4° of λ Ori.

the slope of the data points between our methods to trend toward unity using the simplified equation (18), (N^+/N) would need to decrease with radius. But since the trend in N ionization is important at this point, we should also return to equation 17 and remove the simple assumption $(H^+/H) = 1$. Now we see that $(N^+/N)/(H^+/H)$ becomes the factor that must decrease with radius for our methods to agree. This ratio is difficult to isolate with only the lines we present here. The addition of more emission lines maps, such as [O III], [He I], and Hβ, as well as modeling, which will help us examine the changes in ionization state throughout the nebula, are in progress for a future work.

4. SUMMARY

We have presented multiwavelength observations of Hα, [S II], and [N II] toward the H II region surrounding λ Ori. From these spectra we have produced velocity-resolved maps. The line-ratio maps that compare [S II] and [N II] to that of Hα reveal an increasing trend that is dependent on radius. While variations in these ratios are similar to what is observed in the WIM, the ratios in the H II region have significantly lower values. Using the Hα intensity distribution, we have estimated L_c, the Lyman continuum output from λ Ori, as well as n_e, the average electron density of the H II region. From the widths of Hα and [S II], we derive the spatial structure of the ion temperature (4000 K to 8000 K) and nonthermal velocity (5 km s^{-1} to 10 km s^{-1}) throughout the nebula. We also show a measure of the

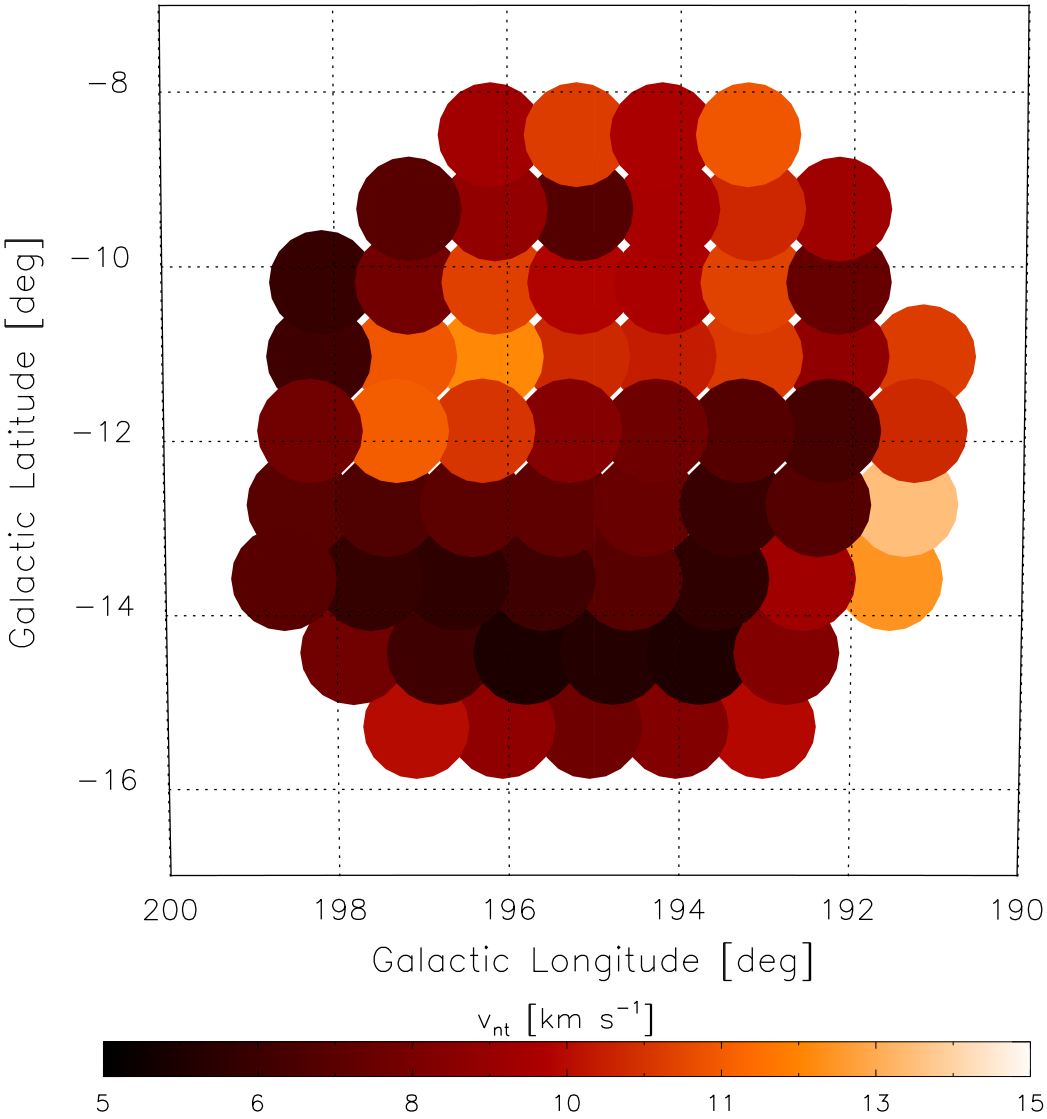

Figure 8. Nonthermal velocity component map of the λ Ori H II region as derived from the observed [S II] and Hα component widths. Velocities are depicted as filled circles that show the coverage and sampling of the WHAM 1°-beam throughout a region within 4° of λ Ori.

electron temperature from the relative intensities of [N II] and Hα and characterize the difference in the two methods of obtaining temperature. Values generally correlate between the two methods and reinforce general trends within the nebula. However, the differences (and trend in differences) between the temperatures determined from these methods is larger than explained by measurement error. For such diffuse, locally-ionized regions, the ionization structure changes significantly throughout the nebula that simple assumptions are insufficient to extract reliable temperatures from the intensity ratio method. Relying on observations alone, we find the widths of S and H emission profiles lead to more robust results. Observations of additional emission lines combined with more sophisticated modeling will allow these data to further constrain the ionization structure.

We acknowledge the long-standing support of WHAM by the U.S. National Science Foundation. The observations and work presented here were supported by awards AST-0607512 and AST-1108911. This research has made use of the SIMBAD database, operated at CDS, Strasbourg, France.

Facilities:

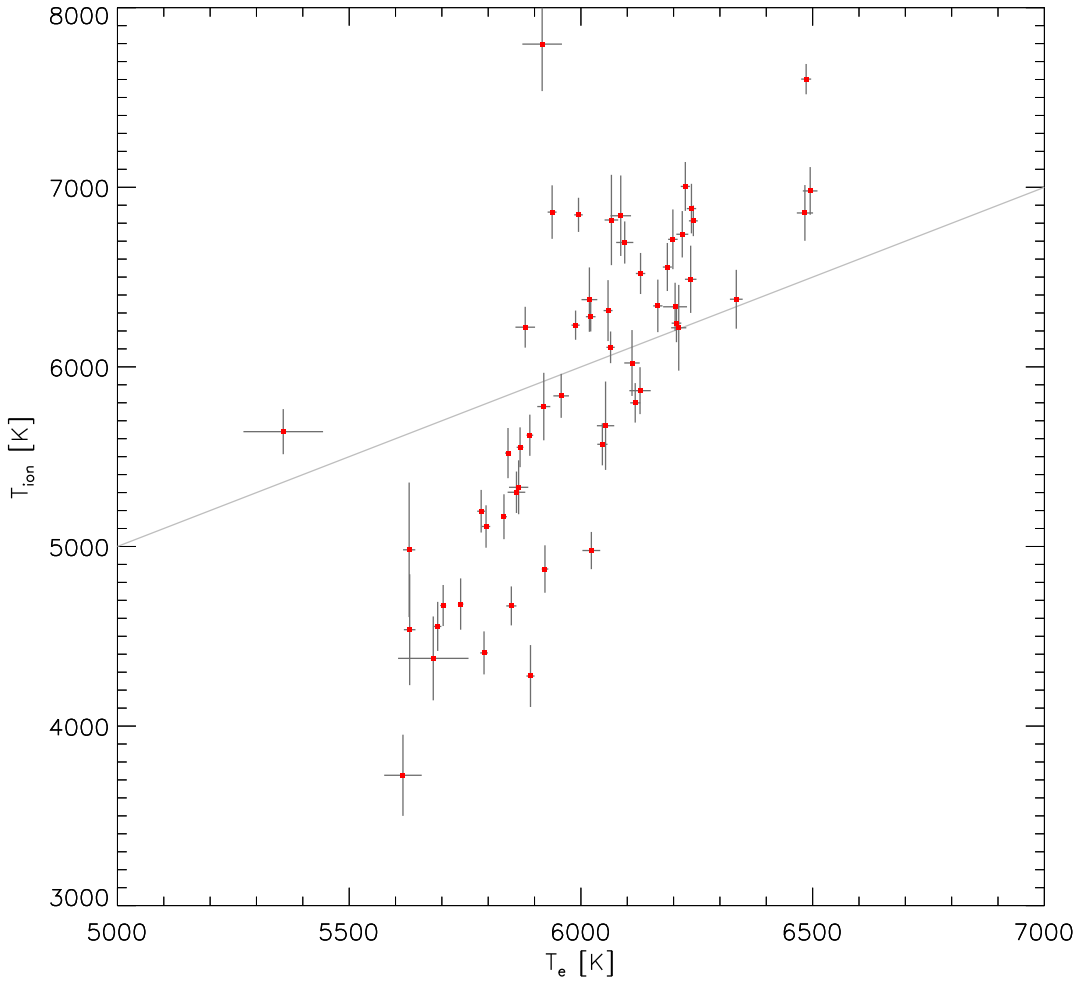

Figure 9. Comparison of empirically derived temperature methods. The ion temperature as derived from [S II] and Hα line widths is plotted against the electron temperature as derived from the [N II]/Hα intensity ratio. For reference, the over-plotted line (*gray*) represents unity. The data points here (*red*) are limited to those within 4° of λ Ori where the H II region dominates emission along the line of sight; blended spectra are excluded (see text). Error bars (*gray*) represent the propagated 1σ uncertainty on the temperatures. Note that the uncertainty on T_e from the measured [N II]/Hα ratio is smaller than the plot symbols for most data points.

Facility: WHAM

REFERENCES

Anders, E., & Grevesse, N. 1989, GeoCoA, 53, 197
Cardelli, J. A., Clayton, G. C., & Mathis, J. S. 1989, ApJ, 345, 245
Cruz-González, C., Recillas-Cruz, E., Costero, R., Piembert, M., & Torres-Piembert, S. 1974, RMxAA, 1, 211
Dennison, B., Simonetti, J. H., & Topasna, G. A. 1998, Publ. Astron. Soc. Australia, 15, 147
Dolan, C. J., & Mathieu, R. D. 2001, AJ, 121, 2124
Dolan, C. J., & Mathieu, R. D. 2002, AJ, 123, 387
Domgörgen, H., & Mathis, J.S. 1994, ApJ, 428, 647
Gaustad, J. E., McCullough, P. R., Rosing, W., & Van Buren, D. 2001, PASP, 113, 1326
Haffner, L. M., Reynolds, R.J., & Tufte, S. L. 1999, ApJ, 523, 223
Haffner, L. M. 2001, in ASP Conf. Ser. 231, Tetons 4: Galactic Structure, Stars and the Interstellar Medium, ed. C. E. Woodward,M.D. Bicay, & J. M. Shull (San Francisco: ASP), 345
Haffner, L. M., Reynolds, R. J., Tufte, S. L., Madsen, G. J., Jaehing, K. P., & Percival, J. W. 2003, ApJS, 149, 405

Hausen, N. R., Reynolds, R. J., Haffner, L. M., & Tufte, S. L. 2002, ApJ, 565, 2, 1060
Heiles, C., Haffner, L.M., Reynolds, R.J. & Tufte, S.L. 2000, ApJ, 536, 335
Howk, J. C., & Savage, B. D. 1999, ApJ, 517, 746
Madsen, G. J., Reynolds, R. J. & Haffner, L. M. 2006, ApJ, 652, 1, 401
Maìz-Appellaniz, J., Walborn, N. A., Galue, H. A., & Wei, L. H. 2004, ApJ, 151, 103
Martin, P. G. 1988, ApJS, 66, 125
Mathieu, R. D. 2008, in Handbook of Star Forming Regions, Volume I: The Northern Sky, ed. B. Reipurth, ASP Monograph Publications, Vol. 4 (Astronomical Society of the Pacific: San Francisco), 757
Meyer, D. M., Cardelli, J. A., & Sofia, U. J. 1997, ApJ, 490, L103
Mierkiewicz, E. J., Roesler, F. L., Nossal, S. M., & Reynolds, R. J. 2006, JASTP, 68, 1520
Nossal, S. M., Mierkiewicz, E. J., Roesler, F. L., Reynolds, R. J., & Haffner, L. M. 2006, JASTP, 68, 1553
Ochsendorf, B. B., Brown, A.G.A., Bally, J., & Tielens, A. G. G. M. 2015, ApJ, 808, 111
Osterbrock, D.E. 1989, Astrophysics of Gaseous Nebulae and Active Galactic Nuclei (Mill Valley: Unitversity Science Books)
Reynolds, R. J. & Ogden P. M. 1982, AJ, 87 , 2
Reynolds, R. J. 1985a, ApJ, 294, 256
Reynolds, R. J. 1985b, ApJ, 298, L27
Reynolds, R. J. 1988, AJ, 96, 670
Reynolds, R. J. & Tufte, S. L. 1995, ApJ, 439, L17
Reynolds, R. J., Tufte, S. L., Haffner, L. M., Jeahnig, K., & Percival J. W. 1998, Publ. Astron. soc. Aust., 15, 14
Reynolds, R. J., Haffner, L. M., & Tufte, S. L. 1999, ApJ, 525, L21
Reynolds, R. J., Haffner, L. M., & Madsen, G. J. 2002, Three-Dimensional Studies of the Warm Ionized Medium in the Milky Way using WHAM, in ASP Conference Proceedings 282: Galaxies: The Third Dimension, eds. M. Rosado, L. Binette, & L. Arias (San Francisco: ASP), 31
Sembach, K. R, Howk, J. C., Ryans, R. S. I., & Keenan, F. P. 2000, ApJ, 528, 1, 310
Scherb, F. 1981, ApJ, 243, 644
Sokolowski, J. 1994, in ASP Conf. Series. 35, Massive Stars: Their Lives in the Interstellar Medium, eds. J. P. Cassinelli & E. B. Churchwell, 540
Tufte, S. L. 1997, PhD thesis, University of Wisconsin-Madison
Vacca, W. D., Garmany, C. D., & Shull J. M. 1996, ApJ, 460, 914